Ceramics International 49 (2023) 1947–1959

Contents lists available at ScienceDirect

Ceramics International

journal homepage: www.elsevier.com/locate/ceramint

Role of A-site (Sr), B-site (Y), and A, B sites (Sr, Y) substitution in lead-free $BaTiO_3$ ceramic compounds: Structural, optical, microstructure, mechanical, and thermal conductivity properties

Mohammed Tihtih [a], Jamal Eldin F.M. Ibrahim [a], Mohamed A. Basyooni [b,c,*], Emese Kurovics [a,d], Walid Belaid [e], Irina Hussainova [f], István Kocserha [a]

[a] Institute of Ceramics and Polymer Engineering, University of Miskolc, H-3515, Miskolc, Egyetemváros, Hungary
[b] Department of Nanotechnology and Advanced Materials, Graduate School of Applied and Natural Science, Selçuk University, Konya 42030, Türkiye
[c] Science and Technology Research and Application Center (BITAM), Necmettin Erbakan University, Konya 42090, Türkiye
[d] Department of Mechanics of Deformed Solids, National Research Tomsk State University, Tomsk, 634050, Russia
[e] Department of Physics, Faculty of Science, Selçuk University, Konya, Türkiye
[f] Tallinn University of Technology, Department of Mechanical and Industrial Engineering, Ehitajate Tee 5, 19086, Tallinn, Estonia

ARTICLE INFO

Keywords:
Sol-gel
Co-doped $BaTiO_3$
Occupation sites
Band gap
Thermal conductivity

ABSTRACT

Strontium and Yttrium-doped and co-doped $BaTiO_3$ (BT) ceramics with the stoichiometric formulas $BaTiO_3$, $B_{1-x}Sr_xTiO_3$, $Ba_{1-x}Y_xTiO_3$, $BaTi_{1-x}Y_xO_3$, $Ba_{1-x}Y_xTi_{1-x}Y_xO_3$, and $Ba_{1-x}Sr_xTi_{1-x}Y_xO_3$ (x = 0.075) noted as BT, BSrT, BYT, BTY, BYTY, and BSrTY have been synthesized through sol-gel method. X-ray diffraction (XRD) patterns of the prepared ceramics, calcined at a slightly low temperature (950 °C/3h), displayed that BT, BSrT, and BYT ceramics possess tetragonal structures and BTY, BYTY, and BSrTY have a cubic structure. The incorporation of the Ba and/or Ti sites by Sr^{2+} and Y^{3+} ions in the lattice of $BaTiO_3$ ceramic and the behaviors of the crystalline characteristics in terms of the Y and Sr dopant were described in detail. The scanning electron microscopy (SEM) images demonstrated that the densification and grain size were strongly related to Sr and Y elements. UV–visible spectroscopy was used to study the optical behavior of the as-prepared ceramic samples and revealed that Sr and Y dopants reduce the optical band gap energy to 2.74 eV for the BSrTY compound. The outcomes also demonstrated that the levels of Urbach energy are indicative of the created disorder following the inclusion of Yttrium. The measurements of the thermal conductivity indicated the influence of the doping mechanism on the thermal conductivity results of the synthesized samples. Indeed, the thermal conductivity of $BaTiO_3$ is decreased with Sr and Y dopants and found to be in the range of 085–2.23 W.m^{-}1. K^{-1} at room temperature and decreases slightly with increasing temperature from 2.02 to 0.73-W.m^{-}1. K^{-1}. Moreover, the microstructure and grains distribution of the BT, BSrT, BYT, BTY, BYTY, and BSrTY samples impacted the compressive strength, hence; the compressive strength was minimized as the grain size decreased.

1. Introduction

In the electronics industry, ceramic perovskite materials are interesting because of their high dielectric constant and provide numerous applications such as sensors, capacitors, power transmission devices, actuators, and high-energy storage devices [1–4]. The vast majority of high ferroelectric materials contain lead which is awful to individuals and the environment because of the toxic effects of lead radiation, such as lead titanate $PbTiO_3$ and lead-zirconium titanate ceramic, PZT [5,6]. To change the lead-based materials, more eco-environmentally friendly materials were examined. The family of Barium titanate perovskite is considered one of the most common lead-free ceramic materials that have many different applications in the electronic industry, including thermistors, capacitors, piezoelectric devices, and the positive temperature coefficient of resistivity, and semiconductors [7–9]. $BaTiO_3$ has a general formula of a perovskite XYO_3 by which Ba represents the X site and Ti occupies the Y site. Thermal management is a crucial part of different and interesting applications in the durability and sincerity of

* Corresponding author. Department of Nanotechnology and Advanced Materials, Graduate School of Applied and Natural Science, Selçuk University, Konya, 42030, Türkiye.
E-mail address: m.a.basyooni@gmail.com (M.A. Basyooni).

https://doi.org/10.1016/j.ceramint.2022.09.160
Received 4 August 2022; Received in revised form 11 September 2022; Accepted 13 September 2022
Available online 17 September 2022

electronic components. Thermal conductivity is one of the most basic thermal transport characteristics of ceramic materials generally and of perovskite materials specifically, and the comprehension of the thermal characteristics of $BaTiO_3$ is essential in designing and effectiveness of numerous applications, including thermal management in the opto-electronic sectors [10]. Moreover, for a better understanding of internal stress affected on multilayer ceramic capacitors (MLCCs), measuring the mechanical properties like compressive strength of doped and co-doped BaTiO3 is crucial for improving the eternity and the reliability of MLCCs [11]. Furthermore, Optical studies are necessary as it is one of the fundamental properties of the $BaTiO_3$ ceramic compound and help obtain information on band gap energy, Urbach energy, and other parameters such as metallization criterion, etc.

In recent years, many studies have been performed on the fabrication of pure and doped BT with high purity and coordinated particle-size distribution. Therefore, different approaches have been developed for the production of doped BT, including the sol-gel [12–14], auto combustion methods [15], solid-state reaction process [16], and hydrothermal [17] to improve the optical, magnetic, and electrical properties of the given BT material. Although, in recent few decades, wet chemical techniques such as the sol-gel process offer many benefits, including manufacturing powders in nano-scale dimensions, good homogeneity, and better stoichiometry control [18–20].

Additionally, it is widely recognized that impurities significantly impact the major properties of $BaTiO_3$ ceramic material. Indeed, adequate ion doping or co-doping is considered an effective and useful technique to improve the structural, microstructural, optical, dialectical, and physical properties of BT. Similarly, the major characteristics of $BaTiO_3$ can easily be modified by doping a cation ion at the X -site and/or Y -site. Typically, the ionic radius can be employed to predict the site occupation of various dopants, e.g. dopants with wide ionic radius and low valence are appropriate to occupy the X-site of Ba^{2+} ($rBa^{2+} = 1.35$ Å) and dopants with high valence and smaller ionic radius are appropriate to occupy the Y-site of Ti^{4+} ($rTi^{4+} = 0.61$ Å) [9]. The substitution site can also be defined X/Y ratio [21]. Moreover, the $BaTiO_3$ can be modified into the semiconductor material by the use of some type of doping which changes the structure and grain size to use in optoelectronic applications [22]. Numerous studies have been performed on the production and investigation of doped BT with different substitutions such as Sr and Ca at the Ba site [23,24] and Fe, Mn, Sn, Zr, and Y at the Ti site to enhance its major properties [25–29]. While La, Sr, Ca, Co, Fe, Mn, and Ni co-doping at both Ba and Ti sites have been carried out for piezoelectric, optical, and magnetic properties of $BaTiO_3$ [30–33]. Besides that, recently, Sr^{2+} and Y^{3+} modified BT materials have received much interest as technologically crucial lead-free ferroelectric materials [23,25,34–39]. Nevertheless, to the best of our knowledge, no similar studies were dedicated to the investigation of the optical, thermal conductivity, and compressive strength of Sr and Y co-doped $BaTiO_3$ using the sol-gel method.

In this work, Sr and Y doped and co-doped $BaTiO_3$ ceramics with the following formulas $BaTiO_3$, $B_{1-x}Sr_xTiO_3$, $Ba_{1-x}Y_xTiO_3$, $BaT_{1-x}Y_xO_3$, $Ba_{1-x}Y_xTi_{1-x}Y_xO_3$, and $Ba_{1-x}Sr_xTi_{1-x}Y_xO_3$ (x = 0.075) and noted as BT, BSrT, BYT, BTY, BYTY, and BSrTY, respectively were prepared through sol-gel technique. The calcination and the sintering processes were carried out at 950°C/3h and 1100 °C for 4 h, respectively. Influences of Sr^{2+} and Y^{3+} ions on the phase structure, lattice constants, and microstructure of $BaTiO_3$ were investigated in detail utilizing X-ray diffraction and SEM. Energy dispersive spectrum (EDS) was utilized to identify the compositional stoichiometry. UV–visible spectroscopy was utilized to investigate the optical behavior of the prepared samples. Detailed studies of compressive strength properties of BT, BSrT, BYT, BTY, BYTY, and BSrTY samples were thoroughly analyzed as a function of both Sr and Y concentrations and grain size distribution. Moreover, the thermal conductivity of the obtained compounds was investigated as a function of the temperature.

2. Experimental details

2.1. Materials and processing

The Y and Sr doped/co-doped $BaTiO_3$ powders were synthesized via sol-gel technique [13] using Barium acetate trihydrate ($Ba(CH_3CO_2)_2.3H_2O$), Yttrium acetate (C6H9O6Y), Strontium acetate ($C_4H_6O_4Sr$), and Titanium alkoxide Ti $[OCH(CH_3)_2]_4$ as starting materials. Lactic acid (CH_3CH (OH) CO_2H) was employed as a peptizing agent, distilled water as a solvent, and acetic acid to dissolve the acetates.

Various processing procedures were used for the synthesis of BT, BSrT, BYT, BTY, BYTY, and BSrTY ceramic materials, as depicted in Fig. 1. The first stage consisted mainly of preparing a clear solution of Barium, Strontium, and Yttrium acetates individually using distilled water as a solvent, indeed, to prepare 100 ml of the solution at 1 M/L, needs; 25.54g of Barium, Yttrium, and Strontium acetates powders, and a small drop of acetic acid (0.25 ml), then the resulting mixture is continuously stirred at the temperature of 80 °C until a clear transparent solution is produced (Solution A). The next stage consists of the preparation of a clear solution of TiO_2. The synthetizes of 250 ml of 1 M/L TiO_2 solution required; 71.75g of Titanium alkoxide, 150g of distilled water, and 11.25g of lactic acid. A white milky precipitate is produced as quickly as TiO_2 solution is added to the lactic acid while stirring it at 70°C. After around 24 h of continuous stirring, the resultant mixture progressively transforms into an entirely clear sol (Solution B). The next stage includes mixing the previously prepared solutions A and B. To guarantee the homogeneity of the final product, the prepared solutions were mixed with referring to the compositional formulas $BaTiO_3$, $B_{1-x}Sr_xTiO_3$, $Ba_{1-x}Y_xTiO_3$, $BaT_{1-x}Y_xO_3$, $Ba_{1-x}Y_xTi_{1-x}Y_xO_3$, and $Ba_{1-x}Sr_xTi_{1-x}Y_xO_3$ (x = 0.075) with continuous stirring for 5 min. The obtained gel was powdered in a programmable oven at 80°C for 48 h. Then, the xerogel product is ground to break up the powders' agglomeration and improve its reactivity. The powders, after grinding, were calcined at 950°C/3 under a heating rate of 5 °C/min hours using a programmable furnace.

2.2. Instrumentation

To determine the annealing temperature of the BT and BSrTY produced samples, a differential thermal analysis (DTA) and Thermogravimetry (TG)-based thermal analysis was performed on the BT and BSrTY ceramic samples recorded until 1000 °C. X-ray diffractometer (Rigaku Miniflex II) with CuKα (λ = 1.5405 Å) was used for the structural study. A "BRUKER-TENSOR 27 spectrophotometer" was used to investigate Fourier transform infrared (FTIR) spectra. To accomplish a good sinterability of the prepared compounds, the ceramics were formed into pellets by applying 7 tons/cm^2 of pressure using a uniaxial pressure. The samples were then heated at 1100 °C for 4 h. The microstructure investigation of the produced ceramic pellets was demonstrated by SEM; Carl Zeiss EVO MA10 operated at 20 kV. The adjusted transient plane source (MTPS) method was used for thermal conductivity and effusivity measurements of the samples using the default (TCi C-Therm) Thermal Conductivity machine. The compressive strength measurements of the ceramic compounds were captured using a (universal electronic testing machine-WDW-50). Finally, the compressive strength at failure was measured in MPa at a loading speed of 1 mm/min. The UV–vis spectrum was taken using an Ocean Optics QE65Pro UV–is spectrophotometer in diffuse reflection mode.

2.3. Physical characterization

For physical measurements including linear shrinkage bulk density, water absorption, apparent and, porosity, the calcined powders at 950 °C for 3 h were first uniaxially pressed at a pressure corresponding to 7 tons to create pellets (about 20 mm in diameter and 5 mm in height).

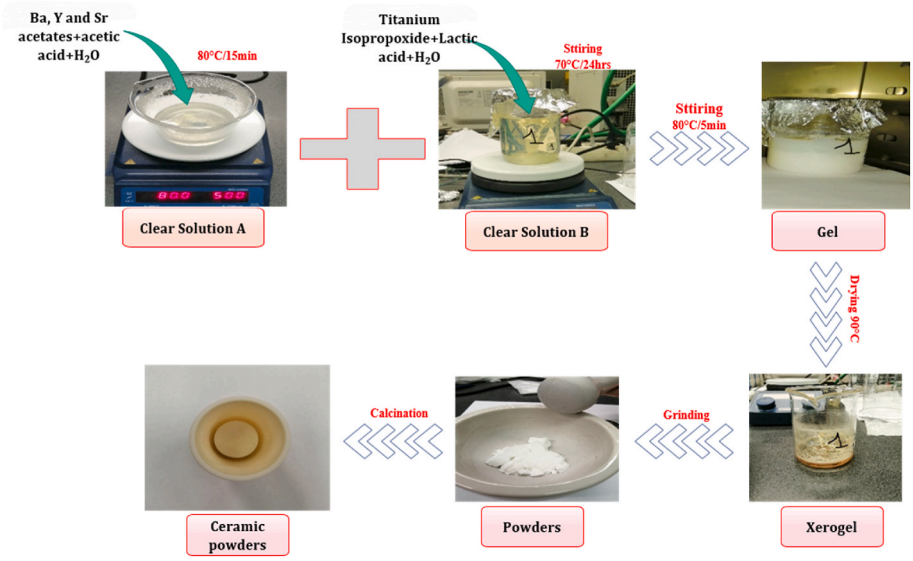

Fig. 1. Flowchart Synthesis of the prepared powders produced via sol-gel method.

As a binder, a small drop of polyvinyl alcohol (PVA) was utilized. to achieve good sinterability of the produced samples at relatively low temperatures, all the samples were sintered up to 1100 °C for 4 h under 5 °C/min as a heating rate to create strong, massive, and dense ceramics. The Archimedes approach was used to assess the bulk density, apparent porosity, and water absorption of the sintered ceramic samples by ASTM C20 [44]. In this technique, the sintered samples were boiled for 2 h in the hot water bath (at 80 °C), then the saturated and suspended weights of pellet ceramics were registered. The subsequent formulas were employed to calculate the bulk density, apparent porosity, and water absorption (noted as B.D, A.P, and W.A, respectively) of different samples:

$$\text{Bulk density } (B.D) = \frac{W_d}{W_w - W_s} \tag{1}$$

$$\text{Apparent porosity } (A.P) = \frac{W_w - W_d}{W_w - W_s} \times 100 \tag{2}$$

$$\text{Water absorption } (W.A) = \frac{W_d}{W_w - W_d} \times 100 \tag{3}$$

Where W_s, W_d, W_w, and are suspended, dry, and, wet weights, respectively.

According to ASTM C326 the linear shrinkage (L.S) was assessed and computed using the following equation [44,45]:

$$\text{Linear shrinkage } (L.S) = \frac{l_0 - l_1}{l0} \times 100 \tag{4}$$

where the sample's pre-sintering and post-sintering lengths are l_0 and l_1, respectively.

3. Results and discussion

3.1. 1. TGA and DTA study

Fig. 2 illustrates the TGA and DTA-based thermal decomposition graphs of BT and BSrTY xerogel. The uncalcined samples were exposed to thermal degradation at temperatures between 22 and 1000 °C under a rate of 5 °C/min. According to the thermal study, the overall mass loss was around 37%, subdivided into 4 steps. The initial weight loss (about 5% for undoped $BaTiO_3$ and ~6% for BSrTY) was found at approximately 26–229°C, related to an endothermic mechanism associated with lactic acid excess and vaporization of water. In the next stage of weight loss, where the largest weight loss was observed. Although TG-curve predicted that the mass of BT and BSrTY would decrease by around 25% and 23.9%, respectively, in the range of temperatures of 229–557°C and 229–550°C, the mass loss in this step can be due to the degradation of the Ba–Ti organic matter and to the deformity of the gel structure. Additionally, this process may also be brought on by the continued combustion of organic materials like $(Ba, Sr)_2Ti_2O_5CO_3$ [46]. The presented endothermic peaks in the DTA spectra at the temperature

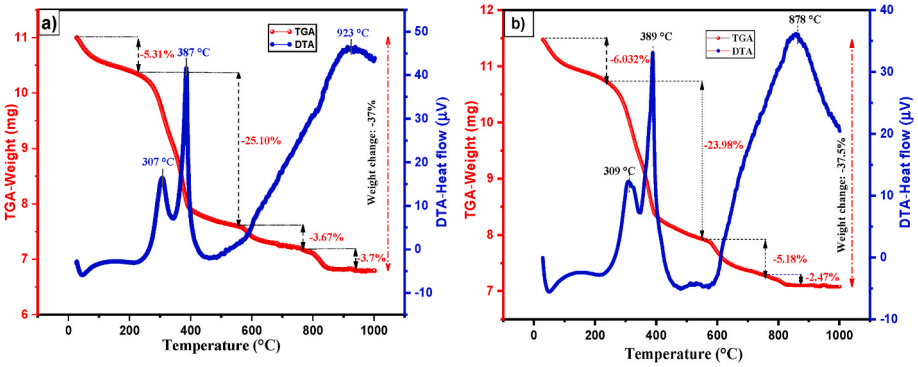

Fig. 2. TGA and DTA curves of the uncalcined (a) $BaTiO_3$ and (b) BSrTY.

range of 307–389 °C are related to the vaporization of leftover organic matter. The third step (557–782°C) ~3% of mass loss and(550–764°C) ~5% for BT and BSrTY respectively, are due to the creation of the intermediate phases. The final stage was found between 782 and 938°C (about 3%) and 764–874°C (2%). This step is corresponding to the crystallization of BT and BSrTY, ceramic samples. Furthermore, the observed exothermic peaks at ~878°C and ~923°C in the DTA spectra are attributed to the decomposition of the carbonate phase. The present study found that the ceramic samples' phase formation temperature is around 950°C.

3.2. X-ray diffraction

The phase formation and the crystallinity are discussed using X-ray diffraction (XRD) analysis. The XRD patterns of BT, BSrT, BYT, BTY, BYTY, and BSrTY are presented in Fig. 3a. No additional peaks were observed in the XRD patterns, which confirms the entire incorporation of 7.5%Sr and 7.5%Y as dopant ions in the $BaTiO_3$ system. Wang et al. [47] produced $BaTi_{1-x}Y_xO_3$ (x =0–0.03) ceramics through a solid-state reaction process and identified the appearance of $BaTi_2O_5$ as an impurity phase. The secondary phase $Y(OH)_3$ was also seen in the XRD patterns of sol hydrothermally treated Y-modified $BaTiO_3$ powders (Y content such as x =0–0.03) [48]. The close observation of the XRD pattern by zooming in on the peak (101) (Fig. 3b) over a range of $30° < 2\Theta < 34°$; displays a shift of the peak (101) initially to lower angles for BSrT, BYT, and BTY. A displacement of Ba^{2+} by Y^{3+} ions into the $BaTiO_3$ lattice leads to a decrease in the volume (V), while the substitution of Y^{3+} into Ti^{4+} ions increases the volume of the unit cell. Therefore, this shift of the peaks to lower angles (BSrT, BYT, and BTY) can be attributed to Y^{3+} ions occupying both Ba^{2+} and Ti^{4+} lattice sites, especially with a preference for the occupation of Ti sites, which may lead to the generating of oxygen vacancies. In the case of BYTY and BSrTY, where a shift of the peaks to the higher 2θ angles was detected, this tendency is reversed; Both Ti and Ba sites are still occupied by Y^{3+}. However, Ba-sites are now more frequently occupied, which in this case results in a significant decrease of the oxygen vacancies as Y behaves as a donor [49]. Moreover, in both cases, barium substituted by strontium in $BaTiO_3$ ceramic (twelve oxygen atoms surround the Ba atom) caused a decrease in the volume(V) and lattice parameters. This outcome demonstrated that Sr^{2+} ions are properly incorporated into Ba^{2+} sites in BSrT and BSrTY systems [50]. Furthermore, the shrinkage within the lattice parameters could be justified by the substitution of Ba^{2+}, which has a higher ionic radius (1.61 Å) by the lower ionic radius Sr^{2+} (1.44 Å). This also unequivocally demonstrates the substitution of Ba^{2+} sites by Sr^{2+} ions without having the option of doing so in Ti^{4+} sites, since Ti^{4+} has an ionic radius of 0.61 Å, which is significantly lower than that of Ba^{2+} and Sr^{2+}.

In XYO_3 perovskite structure, X ions and Y ions are surrounded by 12 and 6 oxygen ions, respectively. Indeed, the modification of Ti^{4+} ions by Y^{3+} ones leads to an expansion of the cell volume (V) and to the generation of oxygen vacancies to balance out the charge imbalance. As a result of the valence state of the doped atoms, two cases can be taken into consideration.

(i) The charge imbalance is compensated by oxygen vacancies in the acceptor dopants because their ionic charge is lower than that of the substituted ion [51,52].
(ii) Higher-ionic-charge donor dopants. In this regard, X- and/or Y-vacancies ($4X^{2+}+Y^{4+}\Rightarrow 4Y^{3+}V_Y$; $3X^{2+}\Rightarrow 2Y^{3+}+V_X$, where X = Ba and Y═Ti) are created to maintain the charge balance. This behavior of the cell volume and lattice constants, specifically the shrinkage in parameter c, in the 3 cases BYT, BTY, and BSrTY can be interpreted by the generation of oxygen vacancies along the C axis [53].

The Fullprof program was used to carry out the structural refinement. Hence, R values (R_{Bragg}, R_p, R_{wp}, Rexp, R_F and χ^2) are typically used to evaluate the quality of structural refinement [54]. After these samples were refined, the numbers of χ^2 and R values were obtained (see Table 1). Fig. 4 shows the Rietveld refinement of BT BSrT and BYT, BTY, BYTY, and BSrTY ceramics powders calcined at 950°C for 3h. The results from X-ray diffraction for all compositions demonstrate the existence of only a single-phase perovskite structure, as clearly seen from the sharp diffraction peaks. In addition, the Refinement parameters confirmed that the BT, BSrT, and BYT compositions belong to tetragonal symmetry, while the BTY, BYTY, and BSrTY compounds confirmed they have cubic structure and a space group of Pm3 m with no apparent secondary phase is detected.

The crystallite sizes were calculated by using Scherrer's formula [55, 56];

$$D = k\lambda/B\cos\theta \quad (5)$$

Where D is the grain size, B is the full width at half the maximum of the diffraction peak, θ is the Bragg diffraction angle, *k* is a dimensionless shape factor, with a typical value of 0.9, and λ is the X-ray wavelength. The estimated crystallite size was found to be in the range of 14–31 nm (Table 1), on which this parameter frequently decreases compared to pure $BaTiO_3$.

The lattice strain was calculated using Wilson's equation [57,58];

$$\beta\cos\theta = 4\varepsilon\sin\theta + 0.9\lambda D \quad (6)$$

Where λ is the wavelength of Cu Kα, D is the crystallite size, β is the full width at half maximum (FWHM), θ is the peak position, and ε is the strain. The obtained strain value is increased with Y and Sr dopants due to the shrinkage changes in the volume cell.

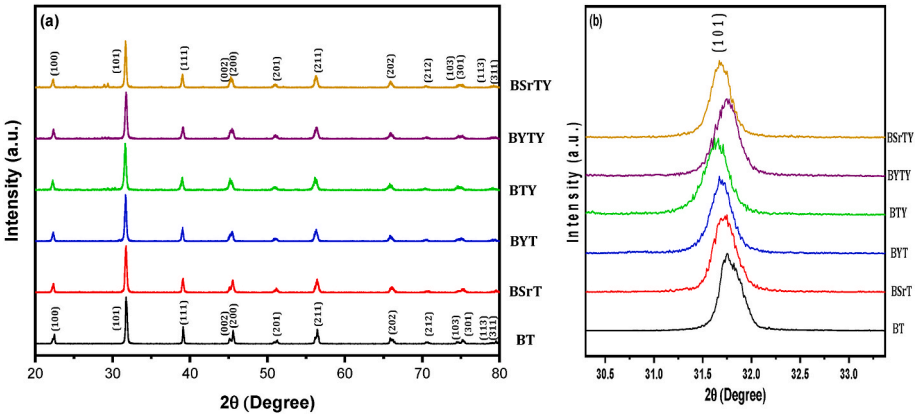

Fig. 3. (a) XRD pattern of BT, BSrT, BYT, BTY, BYTY, and BSrTY ceramics heat-treated at 950°C for 3h **(b)** Shifting of the peak (101).

Table 1
Effect of doping on some properties of $BaTiO_3$.

Material	Synthesis method	Calcination temperature (°C)	Structure	Band gap (eV)	Thermal conductivity ($W.m^{-1}.K^{-1}$)	Ref.
$BaTiO_3$	Solid-state reaction	1100, 4h	Tetragonal	3.3	2.26	[40]
$Ba_{0.99}Bi_{0.01}TiO_3$	Sol-gel	800, 3h	Tetragonal	3.0	–	[13]
$Ba_{0.75}Sr_{0.15}TiO_3$	Sol-gel	950, 3h	Tetragonal	–	3.72	[41]
$BaTi_{0.8}Fe_{0.2}O_3$	sol-gel auto combustion	900, 2h	Tetragonal	3.11	–	[42]
$BaTi_{0.72}Y_{0.28}O_3$	Sol-gel	1050sc, 3h	Tetragonal	2.87	1.97	[43]
$BaTi_{0.985}Co_{0.005}Nb_{0.01}O_3$	Solid-state reaction	1100,5h	Hexagonal	2.98	–	[30]

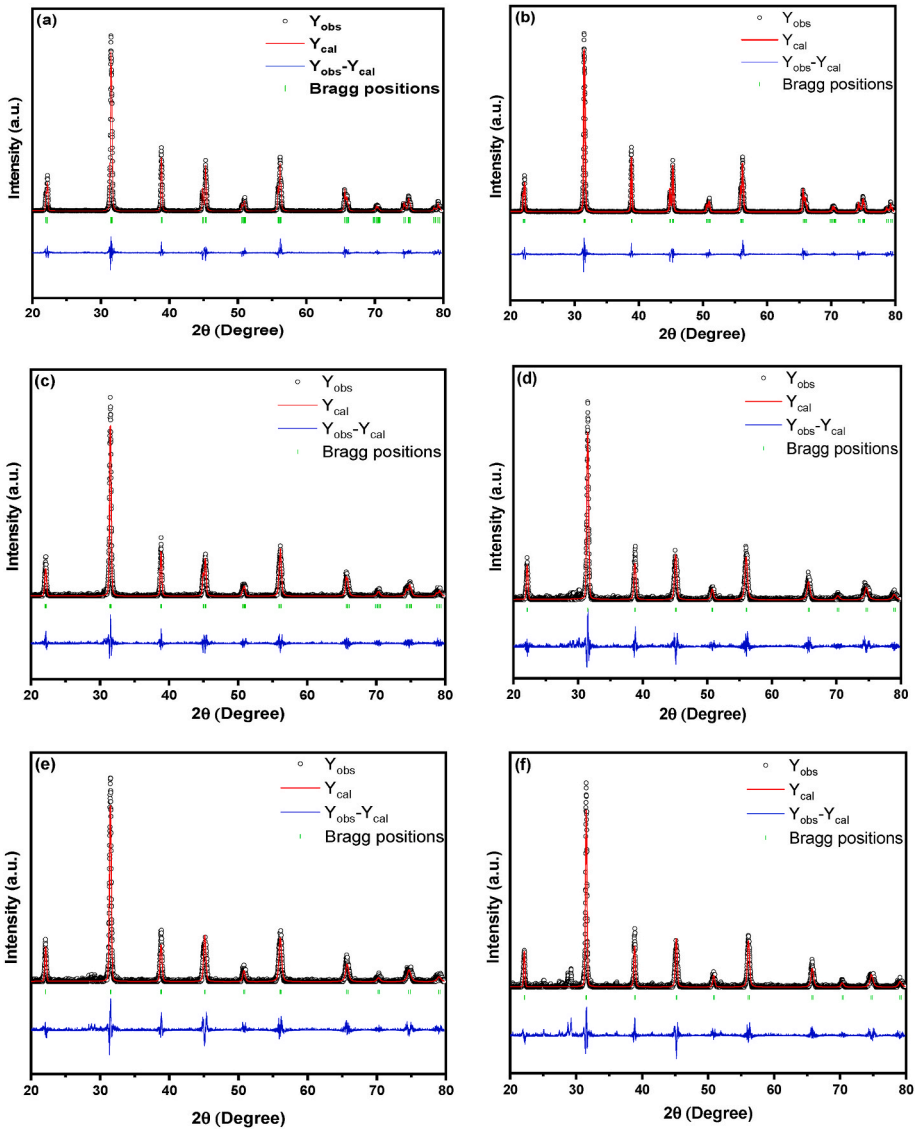

Fig. 4. Structural refinement using the Rietveld method of (a) BT, (b) BSrT, (c) BYT, (d) BTY, (e) BYTY, and (f) BSrTY ceramics.

3.3. FTIR investigation

The Fourier transform infrared spectroscopy (FT-IR) spectrum of BT, BSrT, BYT, BTY, BYTY, and BSrTY powders in the wavenumber range from 450 to 4000 cm^{-1} are displayed in Fig. 5. These spectra show two sets of absorption bands. The first one is characterized by a wide band in the low-frequency range from 460 cm^{-1}–723 cm^{-1}, associated with the vibrations of the TiO_6 octahedron. Moreover, all the samples show the molecular fingerprint of $BaTiO_3$, as revealed by the Ti–O–Ti and Ti–O bonds in the range of 460 cm^{-1} to 723 cm^{-1}. The absorption peaks for the same mode of BT, BSrT, BYT, BTY, and BYTY, were obtained at around 460, 463, 465, 467, 470, and 470 cm^{-1}, respectively. The incorporation of Sr or/and Y into the $BaTiO_3$ lattice moved the characteristic peak of Ti–O to higher energy values. In our samples, the incorporation of Sr^{2+} and Y^{3+} ions into Ba^{2+} and Ti^{4+} sites influenced the binding distance between Ti^{4+} and O^{2-} ions resulting in a high binding strength [59,60]. In addition, the observed bands in the range of 1430 cm^{-1} to 1550 cm^{-1} could be contributed to the symmetrical and antisymmetric vibrations (stretching of carboxyl groups bound to barium and/or titanium (COO^-)). The presented results are, therefore, in good accordance with the reported analysis in the literature [59]. The observations made on infrared spectra agree well with those revealed by

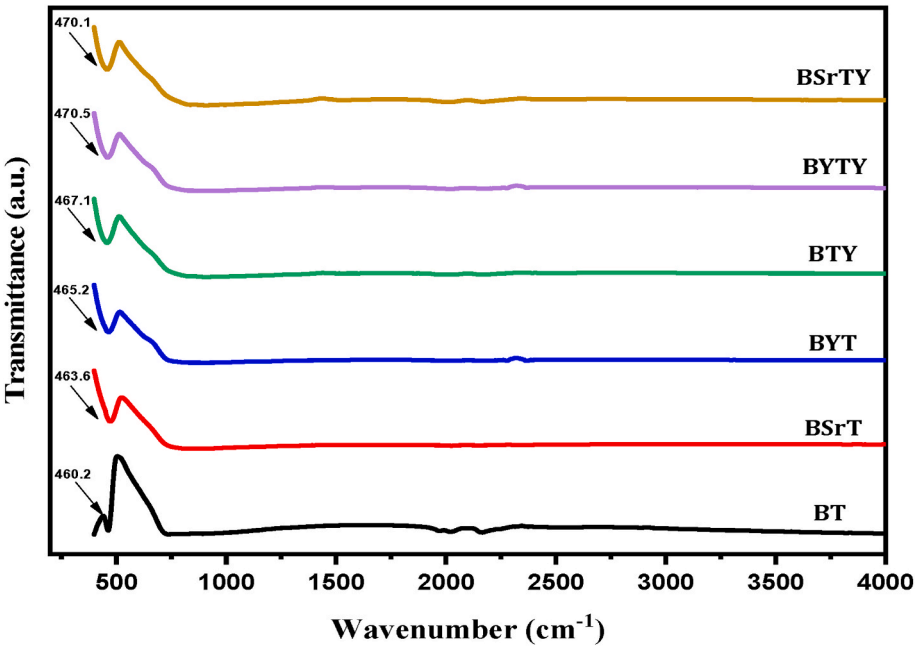

Fig. 5. FTIR spectrums of the BT, BSrT, BYT, BTY, BYTY, and BSrTY ceramic samples.

XRD analysis.

3.4. SEM and EDS analysis

The morphology and the microstructure of the obtained samples were analyzed using SEM. The micrographs provided by the scanning electron microscopy of BSrT, BYT, BTY, BYTY, and BSrTY sintered at 1100°C for 4 h are given in Fig. 6. They show that the ceramics are slightly dense, homogenous, and have irregularly shaped grains in flat block form (BSrT, BYT, BTY, BYTY) and with fine size and almost spherical shaped particles in the case of BSrT. The average grain size decreased under doping from around 4.6 μm (pure sample) [41] to around 0.51 μm (sample with BSrTY) (Table 2). It can be noticed that the above-recorded values relative to the sintered pellets are higher than those of the crystallite sizes of the calcined powders due to the sintering process, which enhances the mechanical resistance of the samples. The observed pores in the ceramic images could be attributed to the rapid cooling as was studied by Niesz et al. [61].

The characterization by X energy dispersive spectroscopy (EDS) of the sintered samples is given in Fig. 6. These results confirm the presence of Ba, Sr, Y, Ti, and O elements, which indicate that the BSrT, BYT, BTY, BYTY, and BSrTY ceramics are compositionally homogeneous and have

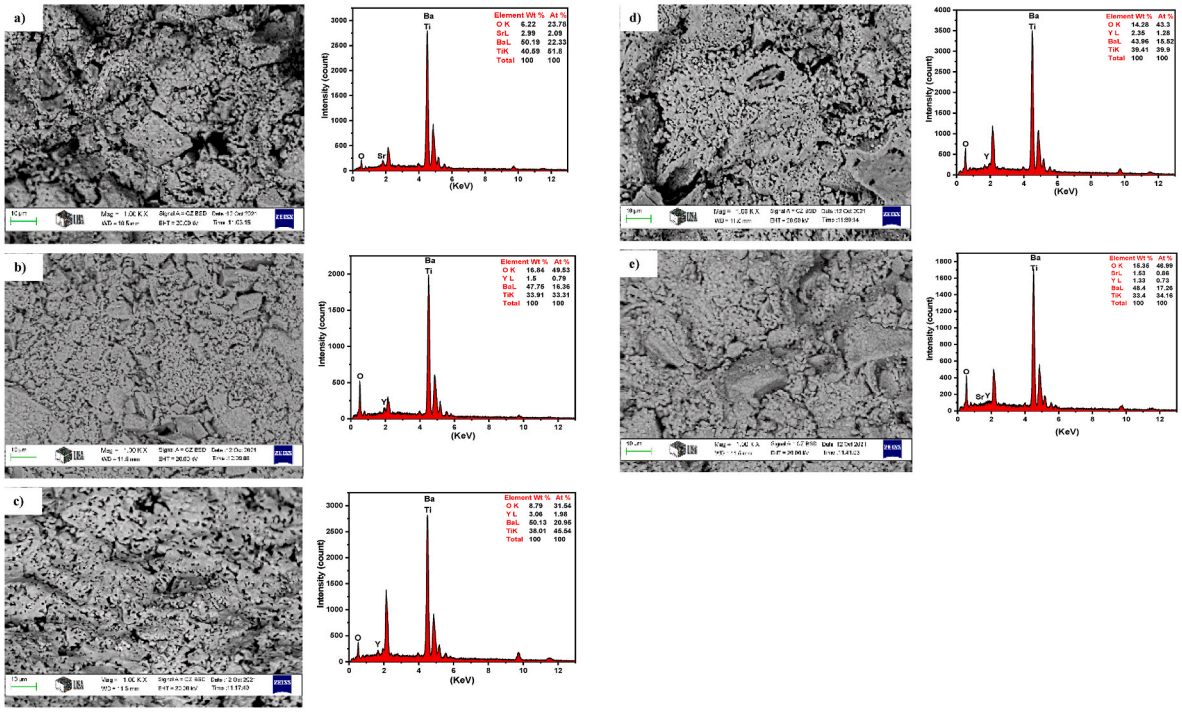

Fig. 6. SEM micrographs and corresponding EDS spectra of a) BSrT, b) BYT, c) BTY, d) BYTY, and e) BSrTY accordingly.

Table 2
Crystallographic data of BT, BSrT, BYT, BTY, BYTY, and BSrTY ceramics using the Rietveld refinement method.

	BT	BSrT	BYT	BTY	BYTY	BSrTY
a (Å)	4.002410	3.995282	4.006745	4.020604	4.019073	4.015099
b (Å)	4.002410	3.995282	4.006745	4.020604	4.019073	4.015099
c (Å)	4.039425	4.024120	4.033381	4.020604	4.019073	4.015099
Volume ($Å^3$)	64.7087	64.23412	64.75192	64.9941	64.91988	64.72749
Structure	Tetragonal	Tetragonal	Tetragonal	Cubic	Cubic	Cubic
Space group	P4mm	P4mm	P4mm	Pm3 m	Pm3 m	Pm3 m
x (Ba)	0			0.5		
y (Ba)	0			0.5		
z (Ba)	0			0.5		
x (Ba, Sr)		0				0.5
y (Ba, Sr)		0				0.5
z (Ba, Sr)		0				0.5
x (Ba, Y)			0		0.5	
y (Ba, Y)			0		0.5	
z (Ba, Y)			0		0.5	
x (Ti)	0.5	0.5	0.5			
y (Ti)	0.5	0.5	0.5			
z (Ti)	0.48347	0.47010	0.51980			
x (Ti, Y)				0	0	0
y (Ti, Y)				0	0	0
z (Ti, Y)				0	0	0
x (O1)	0.5	0.5	0.5	0.5	0.5	0.5
y (O1)	0.5	0.5	0.5	0	0	0
z (O1)	0.05854	0.02015	0.02323	0	0	0
x (O2)	0.5	0.5	0.5			
y (O2)	0	0	0			
z (O2)	0.51642	0.51500	0.53198			
R_{Bragg}	5.027	6.786	7.30	12.31	11.66	10.52
R_p	17.3	23.8	24.5	31.8	30.2	33.4
R_{wp}	26.5	32.2	33	39.7	37.8	42
R_{exp}	22.15	40.95	39.3	40.18	38.47	38.69
R_F				7.89	7.64	7.32
χ^2	1.43	0.61	0.70	0.97	0.96	1.18
Crystallite size (nm) (D)	14	17	18	21	26	31
Strain (ε)	1.27	1.33	1.85	2.21	4.19	4.56

been successfully produced without any contamination. However, It is unable to see the change in the intensity of the distinctive peaks of Ti and Ba since their evolution occurs in the energy region from 4.37 to 4.49 KeV.

3.5. Optical study

UV–Visible Diffuse reflectance spectra of BSrT, BYT, BTY, BYTY, and BSrTY ceramics recorded in the range of 300–1000 nm are shown in Fig. 7. The ceramic samples show an important behavior of visible photons absorption with an absorption maximal of 40% in the wavelength region above 400 nm for the BSrTY sample. The UV spectra of the BSrTY ceramic sample suddenly decrease as a result of the absorption of the visible photons. All the ceramic samples exhibit three separate peaks in the visible region of the spectra, regardless of the Sr and Y sites' occupancy. Moreover, the preference of Sr and Y sites in the BT lattice has a small impact on photon absorption. Indeed, the K-M (Kubelka-Munk) mode monitoring of the diffuse reflectance data was also employed to estimate the optical band gap of the prepared samples.

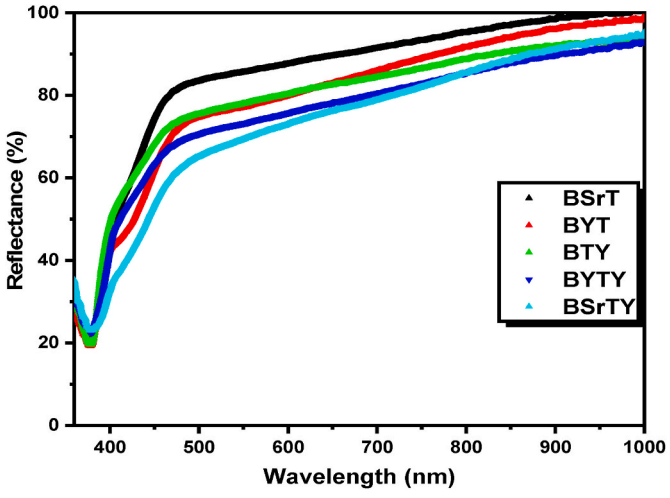

Fig. 7. Reflectance spectra of the as-prepared ceramic samples.

The optical band gap energy (E_g) of BSrT, BYT, BTY, BYTY, and BSrTY ceramic samples was determined with the help of the Kubelkae-Munk method [62]. The Kubelkae-Munk equation is assigned by the following formula:

$$F(R) = \frac{(1-R)^2}{2R} = \frac{k}{S} \quad (7)$$

Where F(R) is the Kubelkae-Munk function or the diffuse reflectance of the low-absorbing standard and $R = R_{sample}/R_{reference}$, S is the scattering coefficient, and k is the coefficient of molar absorption of each ceramic sample. The optical band gap Eg of a semiconductor is estimated by;

$$\alpha h\nu = C_1(h\nu - E_{gap})^n \quad (8)$$

Where $h\nu$ is the photon energy, E_{gap} is the band gap, α is the linear absorption coefficient of a material, n is a constant (n = 1/2 for indirect allowed and n = 2 for direct allowed), and C_1 is a proportionality constant. In this case, photon absorption may stimulate an indirect electronic transition from the bottom of the valence band to a top state in the conduction band. This approach takes place in any region of the Brillouin zone. According to this fact, the optical band gap of all the ceramic samples was calculated and estimated using n = 1/2 in Eq. (8). Finally, using Eq. (7) and with k = the chan2α, we obtain the Kubelkae-Munk modified equation as presented below;

$$[F(R)h\nu]^2 = C_1(h\nu - E_{gap}) \quad (9)$$

Eg values of BSrT powders can be determined with better precision from the plotting of $[F(R)h\nu]^{1/2}$ vs. $h\nu$. The optical band gap energy (Eg) values are 2.97 eV, 3.04 eV, 3.01 eV, 3.03 eV, and 2.74 eV for BSrT, BYT, BTY, BYTY, and BSrTY, respectively (see Fig. 8). In BSrTY material, the conduction band's bottom may gradually be narrow with doping 7.5%Sr in Ba-site and 7.5%Y in Ti-site, resulting in a significantly low band gap energy value compared to the other materials that are doped with only one element (Sr or Y but not both). Moreover, this variation may be due to the changes in the lattice parameters. Tian et al. [63] demonstrated that the BO6 octahedron controls both the top-lying of the valence band and the bottom-lying of the conduction band. The lower-lying conduction states in the structure are influenced by other ions, but these hypotheses typically have only a small impact on the optical characteristics of a certain material. Hence, it may be noted that Ba/Sr ratio has a significant role in the unit cell distortion process. This distortion induces a defect in the band structure, which lowers the intermediate levels in the bandgap region which can be observed from the samples that are mainly doped with Sr content (BSrT and BSrTY). Urbach energies (Eu) have also been estimated for each prepared sample. The sample disorder, which may result from chemical, thermal, polar, or structural flaws, is reflected by the parameter Eu. The relationship between the photon energy and the absorption coefficient at the Urbach edge is given by the following equation [64]:

$$\alpha(E) = \alpha_0.\exp(\frac{E}{E_u}) \quad (10)$$

Where E_u is the Urbach energy, $h\nu$ is the photon energy, α_0 is a constant, and which is weakly affected by temperature.

Since the absorbance is proportional to the absorption coefficient and F(R), accordingly, α can be replaced by F(R). Consequently, we can generally write $F(R) \sim \exp(\frac{E}{E_u})$. The Urbach energy is determined by extraction lnF(R) vs. ($h\nu$). The value of Urbach energy is determined by the fitted lines of the linear slope using the provided equation;

$$\ln F(R) = C + \frac{E}{E_u} \quad (11)$$

The Urbach energy value was estimated by projecting the linear portion of the curve ln(α) as a function of $h\nu$; the Urbach energy was determined and plotted as shown in Fig. 9. It can be observed from the figure that The Urbach energy E_u varies inversely to the behavior of the optical band gap and hence noting the important role played by Y^{3+} and Sr^{2+} ions in generating disorder in the presented ceramic samples. The relationship of the Urbach energy with the band gap and the schematic illustration of the Urbach energy for the as-prepared samples are shown in Fig. 10.

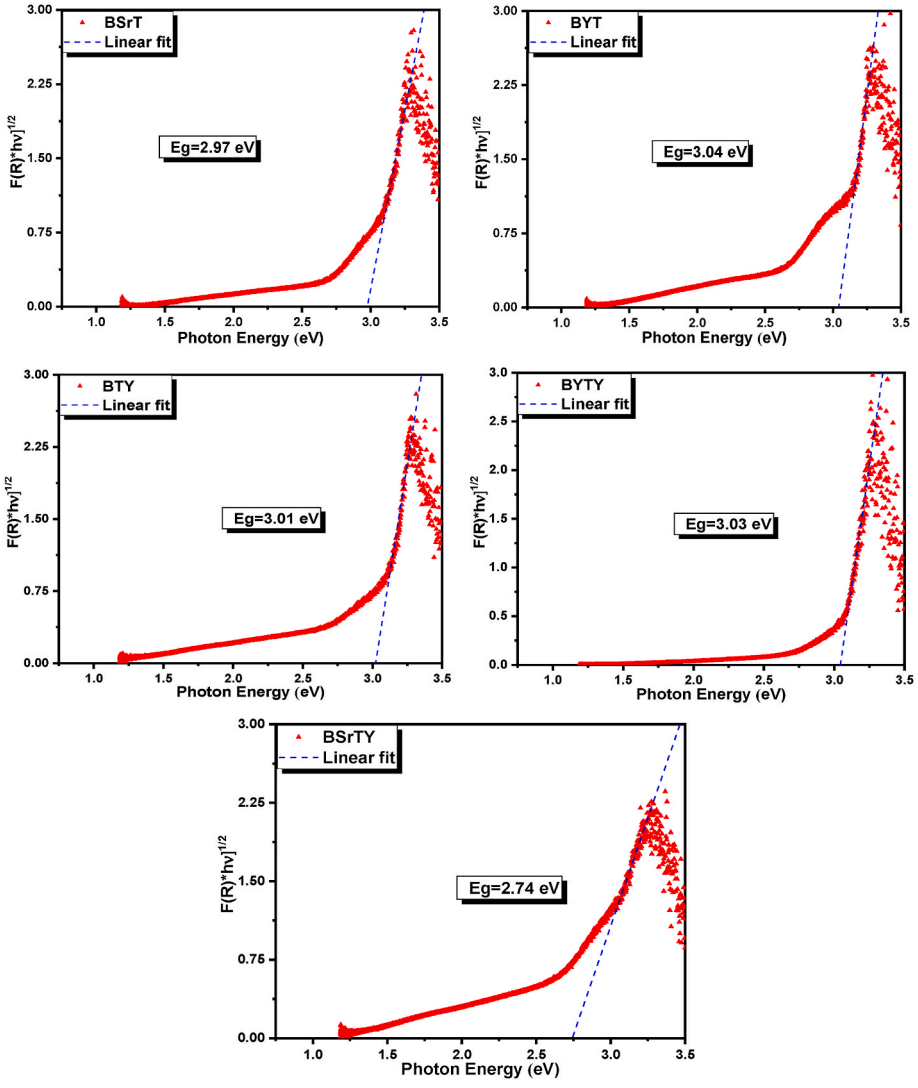

Fig. 8. The plot of $[F(R)h\nu]^{1/2}$ vs. ($h\nu$) for estimating the optical band gap of BSrT, BYT, BTY, BYTY, and BSrTY samples.

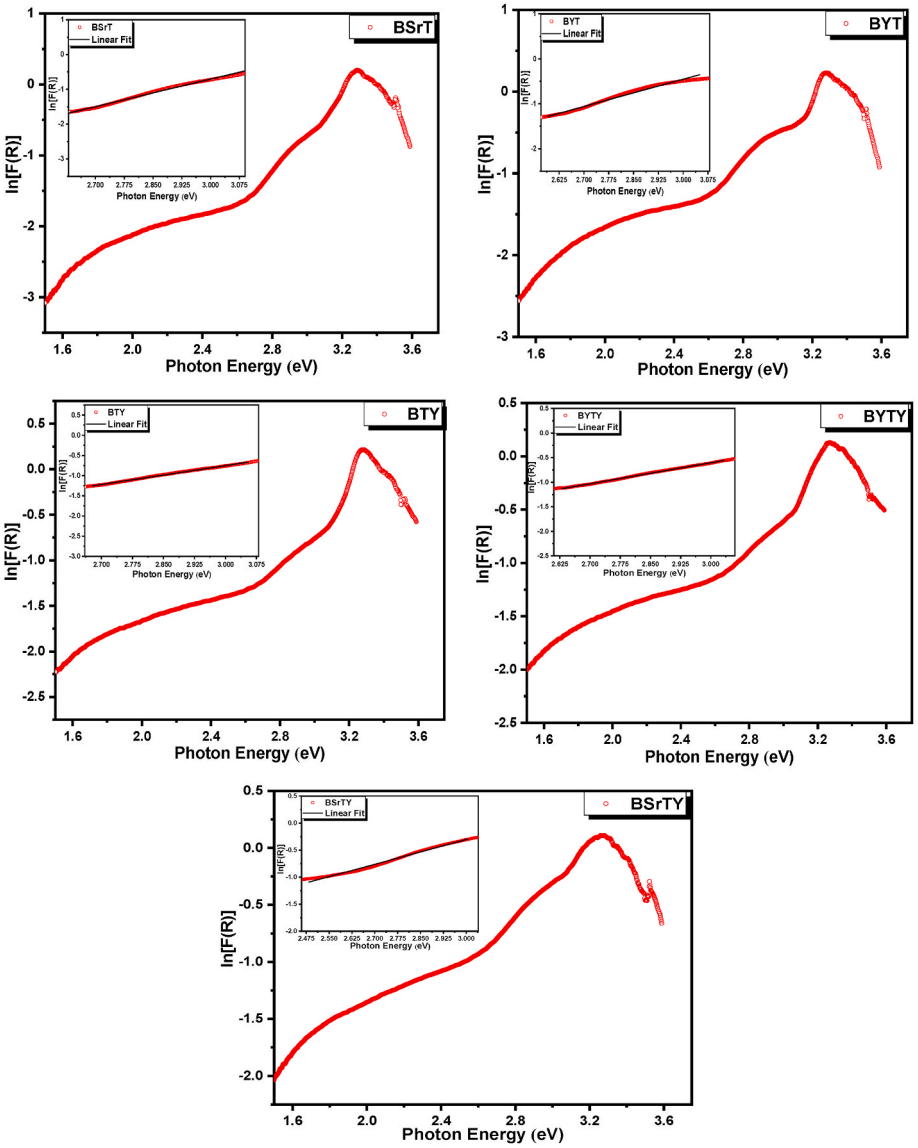

Fig. 9. The plot of ln αvs. hν for determination of the Urbach energy (E_u) for BSrT, BYT, BTY, BYTY, and BSrTY ceramics.

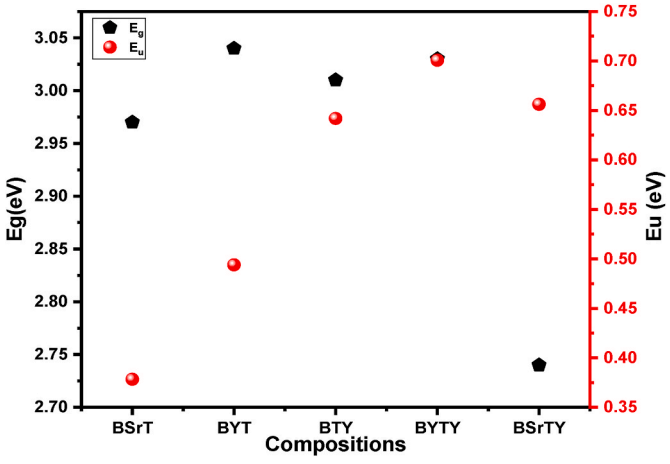

Fig. 10. Urbach energy (Eu) and Band gap energy (Eg) variations for different ceramic compounds.

3.6. Physical analysis

The sintering characteristics of the produced ceramic samples are mainly delicate for manufacturing parameters such as type and amount of dopants, mixing tools, the origin of the raw materials, and the sintering parameters and pressing process. In this research work, the powders were calcined, then pressed and sintered at 1100°C/4h. Fig. 11 shows bulk density (B.D) and apparent porosity (A.P) of BT, BSrT, BYT, BTY, BYTY, and BSrTY ceramic pellets sintered at 1100°C. The addition of Sr and Y as dopants into both Ba and Ti-sites leads to decreasing the apparent porosity and increasing the bulk density [65]. This is due to the symmetric lattice of pure $BaTiO_3$, which makes it less dense as compared with Sr and Y doped-BT. Moreover, in the case of BYTY and BSrTY ceramic samples, the pores are easily enclosed in the grain since the grain boundary moving speed is higher than the pores moving speed, which increases the bulk density of the co-doped $BaTiO_3$ samples. Furthermore, due to the grain boundary scattered at 1100°C and the sintering process that suffuses the pores causing the densification in the resultant composition. This is also indicated through the Linear shrinkage (L.S) measurement, as shown in Fig. 11.

Durability is one of the most significant factors of ceramic materials; it is thought to be closely related to compressive strength and level of

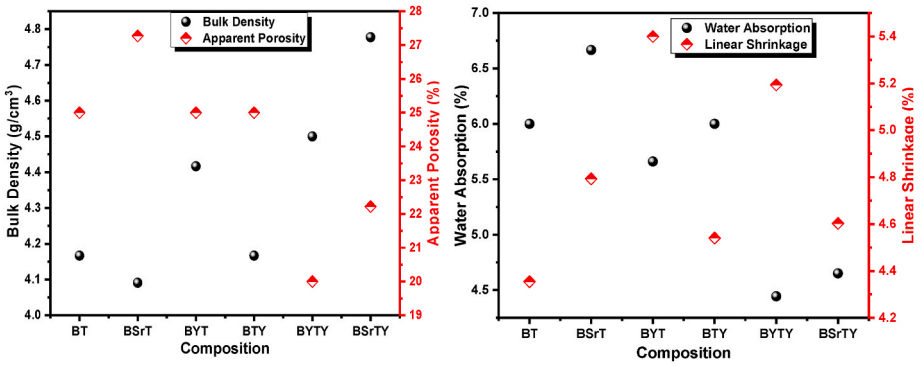

Fig. 11. Physical characteristics of BT, BSrT, BYT, BTY, BYTY, and BSrTY ceramic samples sintered at 1100°C.

water absorption. Indeed, water absorption is an important parameter in exhibiting its environmental toughness [44]. Fig. 11 displays the water absorption and linear shrinkage of BT, BSrT, BYT, BTY, BYTY, and BSrTY samples showing their opposite behaviors. Knowing that the water absorption is directly linked to the size of the pores, as the material's capacity to absorb decreases with decreasing pore size. In this case, the small pores result in the densification of the resultant ceramic material increases, which leads in decreasing of the water absorption of the co-doped compounds compared to pure $BaTiO_3$, which is also proven by SEM [41]. The lowest value of water absorption was 4.4% and 4.65%, obtained from the co-doped samples BYTY and BSrTY, respectively.

3.7. Thermal conductivity

Table 3 presents a summary of the thermal conductivity measurements of the BT, BSrT, BYT, BTY, BYTY, and BSrTY ceramics recorded at 25 °C and 180 °C. The reported values of the thermal conductivity for undoped $BaTiO_3$ were found to be in the region of 1.2–6.5 $Wm^{-1}K^{-1}$ at ambient temperature [66]. The variation in the behavior of thermal conductivity can be due to different synthesis processes used to prepare perovskite ceramics, different measurement techniques, and the type of dopants modified in a given material. Typically, the contributions of lattice thermal conductivity and electrical thermal conductivity are added to determine the overall thermal conductivity [67]. In this work, the standard thermal conductivity at room temperature carried out on undoped barium titanate ceramic is 2.23 $Wm^{-1}K^{-1}$ which is exactly along the region of the obtained results from the literature [10,40]. Therefore, when materials' thermal conductivities are tested in powdered form, they are much lower than in bulk form—by up to an order of magnitude. The heat transfer efficiency in powders is highly reliant on the packing density, interface, contacts, porosity, and composition of the particles. The thermal conductivity for undoped BT is decreased with Sr and Y dopants content and found to be in the range of 085–2.23 $W.m^{-}1. K^{-1}$ at room temperature and decreases slightly with increasing temperature from 0.73 to 2.02 $W.m^{-}1. K^{-1}$. This change is due to the variation in the strength of the atoms' bonds [68]. Indeed. Sr and Y doped samples show a systematic decrease of the thermal conductivity with doping and increasing temperature, indicating that the phonon–-phonon scattering is dominant in the considered temperature range. The

Table 3
The average Grain size of the BSrT, BYT, BTY, BYTY, and BSrTY compounds.

Samples	Grain size (μm)
BSrT	4.1
BYT	3.7
BTY	3.3
BYTY	0.9
BSrTY	0.5

Table 4
Thermal conductivity of the as-prepared samples.

Sample	Thermal Conductivity (W/mK)	
	25 °C	180 °C
BT	2.23	2.02
BSrT	1.32	1.05
BYT	0.9	0.9
BTY	0.95	0.85
BYTY	0.6	0.35
BSrTY	0.85	0.73

thermal conductivities of the Sr, Y co-doped samples are lower and become less dependent on the temperature. This is caused by the relative increase of the temperature-independent phonon–impurity scattering. The amount of the thermal conductivities are, BSrTY < BYTY < BTY < BYT < BSrT for the doped samples, which is the same sequence as that of the lattice parameters. Abeles showed that the reciprocal relaxation time of phonon–impurity scattering is proportional to the difference between the dopant and matrix ion of both the ionic radius and the mass [69]. The Y ion has a slightly smaller ionic radius than Sr [70] and has less than half of the atomic mass of Sr, which indicates the phonon–impurity scattering is mainly produced by the lattice distortion caused by the difference in ionic radii, not by the mass difference Therefore, thermal conductivity decreases with the decrease of ionic radius, and then, reaches a lower limitation when the ionic radius is small enough. The ionic radii of all these doped elements are smaller than that of the Ba ion (1.61 Å). The smaller the ionic radius is, the larger the difference between the doped ion and Ba and/or Ti ion would be, which might introduce larger distortion into the lattice and thus reduce the lattice thermal conductivity. To retain the lattice structure, such distortion cannot be introduced infinitely, resulting in the lower limitation of the thermal conductivity value which is the case for BYTY and BSrTY co-doped samples. Furthermore, the described Oxygen vacancies in the XRD analysis also played an important role in the variation of the thermal conductivity, which can be seen from Table 3 that the samples that show lower values were the ceramics that are doped with Y content. Further, the reduction between Ti–O bonds made the bond slightly strong. These variations in the bond tendency's strength are more effective for thermal conductivity in the system than the scattering of the point defect. In addition, from the SEM micrographs (Fig. 6), the surface of the analyzed samples showed a structure unavailable to small pores. The thermal conductivity decreases as the surface complexity of the particles increases. All the samples have sizable micropores, which resulted in low heat conductivity values (see Table 4).

3.8. Mechanical properties

Fig. 12 displays the compressive strength of the BT, BSrT, BYT, BTY, BYTY, and BSrTY ceramics recorded. It can be observed from Fig. 12 that the compressive strength value of the as-prepared ceramic samples is

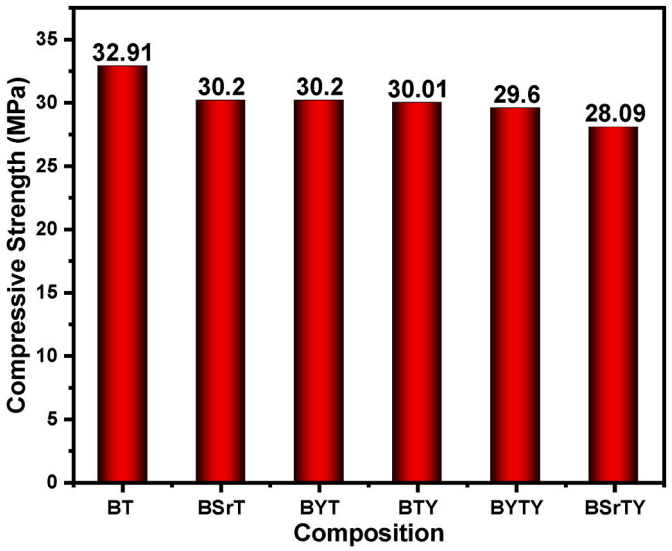

Fig. 12. Histogram of the compressive strength of the as-prepared BSrT, BYT, BTY, BYTY, and BSrTY samples.

32.91, 30.2, 30.2, 30.01, 29.6, and 28.09 MPa for BT, BSrT, BYT, BTY, BYTY, and BSrTY, respectively, however, the compressive strength results revealed irrelevant changes when using Sr and Y dopants in $BaTiO_3$. The strength of the cohesion between the grains of the ceramic compounds, in addition to the shape and the particle sizes, mainly depends on the pores, the separation of the particles, and shrinkage. High compressive strength results from the irregular grain shape distribution that is nearly attached to the particles [71]. The higher compressive strength value observed (32.91 MPa) was probably due to the shape of the irregular flat block grains forming, which greatly weakened the atom bonds. Additionally, based on the scanning electron microscopy examination, the microstructure of Sr, Y doped-co-doped $BaTiO_3$ samples differs significantly. For flat blocks of BSrTY (0.5 μm average grain size), the measured values of the pores' diameter have pores that are barely identical in shape and size, which are in both cases in flat block form. Further, the pores in undoped BaTiO3, which has a larger particle size, are likewise larger and have a shape of a flat block. The highest value of the compressive strength was found for undoped $BaTiO_3$ material corresponding to the higher grain size, whereas, the minimum value was 28.09 MPa for BSrTYcompound.

4. Conclusion

$BaTiO_3$, $B_{1-x}Sr_xTiO_3$, $Ba_{1-x}Y_xTiO_3$, $BaT_{1-x}Y_xO_3$, $Ba_{1-x}Y_xTi_{1-x}Y_xO_3$, and $Ba_{1-x}Sr_xTi_{1-x}Y_xO_3$ (x = 0.075) ceramics have been properly synthesized by sol-gel process. The structural, microstructural, chemical compositional stoichiometry, optical, thermal conductivity, and mechanical properties of the prepared samples were studied and described in detail. X-ray diffraction evaluation and Rietveld refinement have shown that BT, BSrT, and BYT ceramic compounds possess tetragonal structure and cubic structure for BTY, BYTY, and BSrTY samples. FT-IR investigations have supported the XRD analysis's results. The SEM analyses revealed that the particles are formed in the shape of flat blocks. EDS investigation revealed that the produced ceramic samples are in a high-purity material without any impurities. The changes in thermal conductivity with Y and Sr dopants can be ascribed to the increase in the distance within Ti -O bonds and due to the change in the strength of the bond between the atoms. UV–vis spectroscopy was used to identify the optical band gap of the ceramics, and it showed a decrease caused by the generation of oxygen vacancies and the introduction of lattice distortions. The examination of the mechanical strength properties indicated that the compressive strength of the BT, BSrT, BYT, BTY, BYTY, and BSrTY ceramics decreases with the Sr and Y dopant contents; this variation in the compressive strength behavior is related to the shape and the grain size of the latter. A higher compressive strength corresponded to the undoped barium titanate, demonstrating that the microstructure of the as-prepared ceramic compounds affects the compressive strength. In micro-optical electro-mechanical systems, the studied materials could function as multipurpose, smart materials by fusing their exceptional physical and optical properties.

Declaration of competing interest

The authors declare that they have no known competing financial interests or personal relationships that could have appeared to influence the work reported in this paper.

Acknowledgments

This work did not receive any funding. The first and corresponding authors would like to thank the Abdus Salam International Centre for Theoretical Physics (ICTP) Trieste TS, Italy for the building discussions and the tremendous multidisciplinary talks and events.

References

[1] H. Kabra, H.A. Deore, P. Patil, Review on advanced piezoelectric materials (BaTiO3, PZT), J. Emerg. Technol. Innov. Res. 6 (2019) 950.
[2] V.T. Rathod, A review of acoustic impedance matching techniques for piezoelectric sensors and transducers, Sensors 20 (2020) 4051, https://doi.org/10.3390/S20144051.
[3] D. Wang, J.S. Chen, Progress on the applications of piezoelectric materials in sensors, Mater. Sci. Forum (2016) 749–756. https://doi.org/10.4028/www.scientific.net/MSF.848.749.
[4] M.A. Basyooni, S.E. Zaki, S. Ertugrul, M. Yilmaz, Y.R. Eker, Fast response of CO2 room temperature gas sensor based on Mixed-Valence Phases in Molybdenum and Tungsten Oxide nanostructured thin films, Ceram. Int. 46 (2020) 9839–9853, https://doi.org/10.1016/J.CERAMINT.2019.12.259.
[5] W. Wang, Y. Jiang, P.J. Thomas, Structural design and physical mechanism of axial and radial sandwich resonators with piezoelectric ceramics: a review, Sensors 21 (2021) 1112, https://doi.org/10.3390/S21041112.
[6] Y. Ma, J. Song, X. Wang, Y. Liu, J. Zhou, Synthesis, Microstructure and properties of magnetron sputtered lead zirconate titanate (PZT) thin film coatings, Coatings 11 (2021) 944, https://doi.org/10.3390/COATINGS11080944.
[7] P. Gupta, S. Sen, Structural, Optoelectronic and Ferroelectric Behavior of A & B Site Modified BaTiO3, 2020.
[8] Y.C. Teh, A.A. Saif, Z.A.Z. Jamal, P. Poopalan, Microstructure study on Gd-doped BaTiO3 sol-gel multilayer thin films using AFM for optoelectronic applications, Adv. Mater. Res. 911 (2014) 251–255, https://doi.org/10.4028/WWW.SCIENTIFIC.NET/AMR.911.251.
[9] D. Hu, Z. Pan, X. Tan, F. Yang, J. Ding, X. Zhang, P. Li, J. Liu, J. Zhai, H. Pan, Optimization the energy density and efficiency of BaTiO3-based ceramics for capacitor applications, Chem. Eng. J. 409 (2021), 127375, https://doi.org/10.1016/J.CEJ.2020.127375.
[10] J. Xing, M. Radovic, A. Muliana, Thermal properties of BaTiO3/Ag composites at different temperatures, Compos. B Eng. 90 (2016) 287–301, https://doi.org/10.1016/J.COMPOSITESB.2015.12.014.
[11] S.-S. Ryu, H.-T. Kim, H.J. Kim, S. Kim, Characterization of mechanical properties of BaTiO3 ceramic with different types of sintering aid by nanoindentation, J. Ceram. Soc. Japan. 117 (2009) 811–814, https://doi.org/10.2109/JCERSJ2.117.811.
[12] M. Tihtih, J.E.F.M. Ibrahim, E. Kurovics, L.A. Gömze, Study of the structure, microstructure and temperature dependent thermal conductivity properties of SrTiO3: via Y3+ substitution, J. Nano Res. 69 (2021) 33–42, https://doi.org/10.4028/WWW.SCIENTIFIC.NET/JNANOR.69.33.
[13] M. Tihtih, J.F.M. Ibrahim, E. Kurovics, M. Abdelfattah, Study on the effect of Bi dopant on the structural and optical properties of BaTiO 3 nanoceramics synthesized via sol-gel method, J. Phys. Conf. Ser. 1527 (2020), 012043, https://doi.org/10.1088/1742-6596/1527/1/012043.
[14] M.A. Basyooni, M. Shaban, A.M. El Sayed, Enhanced gas sensing properties of spin-coated Na-doped ZnO nanostructured films, Sci. Rep. 7 (2017), https://doi.org/10.1038/srep41716.
[15] S. Goel, A. Tyagi, A. Garg, S. Kumar, H.B. Baskey, R.K. Gupta, S. Tyagi, Microwave absorption study of composites based on CQD@BaTiO3 core shell and BaFe12O19 nanoparticles, J. Alloys Compd. 855 (2021), 157411, https://doi.org/10.1016/J.JALLCOM.2020.157411.
[16] E. Song, D.H. Kim, E.J. Jeong, M. Choi, Y. Kim, H.J. Jung, M.Y. Choi, Effects of particle size and polymorph type of TiO2 on the properties of BaTiO3 nanopowder prepared by solid-state reaction, Environ. Res. 202 (2021), 111668, https://doi.org/10.1016/J.ENVRES.2021.111668.
[17] M. Habib, M. Munir, F. Akram, S. Lee, T.K. Song, A. Turak, M.H. Kim, A. Hussain, Structural evolution and electromechanical properties of SrTiO3-modified

Bi0.5Na0.5TiO3–BaTiO3 ceramics prepared by sol-gel and hydrothermal methods, Mater. Chem. Phys. 266 (2021), 124529, https://doi.org/10.1016/J.MATCHEMPHYS.2021.124529.
[18] M. Tihtih, K. Limame, Y. Ababou, S. Sayouri, J.-E.F.M. Ibrahim, Sol-gel synthesis and structural characterization of Fe doped barium titanate nanoceramics, Epa. - J. Silic. Based Compos. Mater. 71 (2019) 190–193, https://doi.org/10.14382/EPITOANYAG-JSBCM.2019.33.
[19] M. Tihtih, J.E.F.M. Ibrahim, M.A. Basyooni, W. Belaid, L.A. Gömze, I. Kocserha, Structural, Optical, and Electronic Properties of Barium Titanate: Experiment Characterisation and First-Principles Study, 2022, pp. 1–11, https://doi.org/10.1080/10667857.2022.2107473.
[20] Y. Ko, Y. Kim, S.Y. Kong, S.C. Kunnan, Y. Jun, Improved performance of sol–gel ZnO-based perovskite solar cells via TiCl4 interfacial modification, Sol. Energy Mater. Sol. Cells 183 (2018) 157–163, https://doi.org/10.1016/J.SOLMAT.2018.04.021.
[21] P.C. Bowes, J.N. Baker, D.L. Irving, Site preference of Y and Mn in nonstoichiometric Ba TiO3 from first principles, Phys. Rev. Mater. 4 (2020), 084601, https://doi.org/10.1103/PhysRevMaterials.4.084601.
[22] S. Pradhan, H. Kaur, M. Jayasimhadri, Photoluminescence and thermal sensing properties of Er3+ doped silicate based phosphors for multifunctional optoelectronic device applications, Ceram. Int. 47 (2021) 27694–27701, https://doi.org/10.1016/J.CERAMINT.2021.06.194.
[23] A. Boubaia, A. Assali, S. Berrah, H. Bennacer, I. Zerifi, A. Boukortt, Band gap and emission wavelength tuning of Sr-doped BaTiO3 (BST) perovskites for high-efficiency visible-light emitters and solar cells, Mater. Sci. Semicond. Process. 130 (2021), 105837, https://doi.org/10.1016/J.MSSP.2021.105837.
[24] N. Zamperlin, R. Ceccato, M. Fontana, A. Pegoretti, A. Chiappini, S. Dirè, Effect of hydrothermal treatment and doping on the microstructural features of sol-gel derived BaTiO3 nanoparticles, Mater 14 (2021) 4345, https://doi.org/10.3390/MA14154345.
[25] Y. Zhao, Q. Wang, J.H. Lv, X. Zhao, C.M. Wang, Dielectric properties and electrocaloric effect of yttrium-modified BaTiO3 ceramics, Ceram. Int. 47 (2021) 18610–18618, https://doi.org/10.1016/J.CERAMINT.2021.03.192.
[26] I.C. Amaechi, A. Hadj Youssef, G. Kolhatkar, D. Rawach, C. Gomez-Yañez, J. P. Claverie, S. Sun, A. Ruediger, Ultrafast microwave-assisted hydrothermal synthesis and photocatalytic behaviour of ferroelectric Fe3+-doped BaTiO3 nanoparticles under simulated sunlight, Catal. Today 360 (2021) 90–98, https://doi.org/10.1016/J.CATTOD.2019.07.021.
[27] W. Peng, L. Li, S. Yu, P. Yang, K. Xu, Dielectric properties, microstructure and charge compensation of MnO2-doped BaTiO3-based ceramics in a reducing atmosphere, Ceram. Int. (2021), https://doi.org/10.1016/J.CERAMINT.2021.07.083.
[28] M. Naveed-Ul-Haq, Exploring Ba(Ti, Sn)O3: an experimental and theoretical study of structural, ferroelectric, electronic, and optical properties, Mater, Today Commun 28 (2021), 102494, https://doi.org/10.1016/J.MTCOMM.2021.102494.
[29] Q. Xu, Z. Li, Dielectric and ferroelectric behaviour of Zr-doped BaTiO3 perovskites, Process, Appl. Ceram. 14 (2020) 188–194, https://doi.org/10.2298/PAC2003188X.
[30] G.M. Osoro, D. Bregiroux, M.P. Thi, F. Levassort, Structural and piezoelectric properties evolution induced by cobalt doping and cobalt/niobium co-doping in BaTiO3, Mater. Lett. 166 (2016) 259–262, https://doi.org/10.1016/j.matlet.2015.12.086.
[31] S. Rajan, P.M.M. Gazzali, G. Chandrasekaran, Electrical and magnetic phase transition studies of Fe and Mn co-doped BaTiO3, J. Alloys Compd. 656 (2016) 98–109, https://doi.org/10.1016/J.JALLCOM.2015.09.199.
[32] K. Madhan, R. Murugaraj, Structural, electrical, and weak ferromagnetic-to-antiferromagnetic nature of Ni and La co-doped BaTiO3 by sol–gel combustion route, J. Sol. Gel Sci. Technol. 951 (95) (2020) 11–21, https://doi.org/10.1007/S10971-020-05311-1.
[33] A. Jain, A.K. Panwar, Synergetic effect of rare-earths doping on the microstructural and electrical properties of Sr and Ca co-doped BaTiO3 nanoparticles, Ceram. Int. 46 (2020) 10270–10278, https://doi.org/10.1016/J.CERAMINT.2020.01.020.
[34] M. Arshad, H. Du, M.S. Javed, A. Maqsood, I. Ashraf, S. Hussain, W. Ma, H. Ran, Fabrication, structure, and frequency-dependent electrical and dielectric properties of Sr-doped BaTiO3 ceramics, Ceram. Int. 46 (2020) 2238–2246, https://doi.org/10.1016/J.CERAMINT.2019.09.208.
[35] S. Yadav, M. Chandra, R. Rawat, V. Sathe, A.K. Sinha, K. Singh, Structural correlations in the enhancement of ferroelectric property of Sr doped BaTiO3, J. Phys. Condens. Matter 32 (2020), 445402, https://doi.org/10.1088/1361-648X/ABA384.
[36] B. Yang, H. Chen, Y. Yang, L. Wang, J. Bian, Q. Liu, X. Lou, Insights into the tribo-/pyro-catalysis using Sr-doped BaTiO3 ferroelectric nanocrystals for efficient water remediation, Chem. Eng. J. 416 (2021), 128986, https://doi.org/10.1016/J.CEJ.2021.128986.
[37] R. Verma, A. Chauhan, K.M. Batoo, R. Kumar, M. Hadi, E.H. Raslan, Structural, morphological, and optical properties of strontium doped lead-free BCZT ceramics, Ceram. Int. 47 (2021) 15442–15457, https://doi.org/10.1016/j.ceramint.2021.02.110.
[38] P. Ren, Q. Wang, X. Wang, L. Wang, J. Wang, H. Fan, G. Zhao, Effects of doping sites on electrical properties of yttrium doped BaTiO3, Mater. Lett. 174 (2016) 197–200, https://doi.org/10.1016/j.matlet.2016.03.110.
[39] S. Mittal, R. Laishram, K.C. Singh, Multi-phase coexistence in yttrium-substituted Ba0.9Ca0.1Zr0.07Ti0.93O3 lead-free piezoceramics, Ceram. Int. 45 (2019) 1237–1245, https://doi.org/10.1016/J.CERAMINT.2018.09.312.
[40] J. Suchanicz, P. Czaja, K. Kluczewska, H. Czternastek, M. Sokolowski, A. Węgrzyn, The Influence of Pb(Mg1/3Nb2/3)O3-doping on the thermoelectric properties of BaTiO3 ceramics, Phase Transitions 91 (2018) 1036–1043, https://doi.org/10.1080/01411594.2018.1506880.
[41] M. Tihtih, J.E.F.M. Ibrahim, E. Kurovics, L.A. Gömze, Synthesis of Ba1−xSrxTiO3 (x = 0–0.3) ceramic powders via sol-gel method: structural, microstructure, thermal conductivity, and compressive strength properties, Cryst. Res. Technol. (2021), 2100106, https://doi.org/10.1002/CRAT.202100106.
[42] P.P. Khirade, S.D. Birajdar, A.V. Raut, K.M. Jadhav, Effect of Fe – substitution on phase transformation, optical, electrical and dielectrical properties of BaTiO3 nanoceramics synthesized by sol-gel auto combustion method, J. Electroceram. 37 (2016) 110–120, https://doi.org/10.1007/S10832-016-0044-Z/TABLES/1.
[43] M. Afqir, M. Elaatmani, A. Zegzouti, A. Oufakir, M. Daoud, Sol–gel synthesis, structural and dielectric properties of Y-doped BaTiO 3 ceramics, J. Mater. Sci. Mater. Electron. 30 (2019) 5495–5502, https://doi.org/10.1007/S10854-019-00843-X/FIGURES/10.
[44] J.E.F.M. Ibrahim, O.B. Kotova, S. Sun, E. Kurovics, M. Tihtih, L.A. Gömze, Preparation of innovative eco-efficient composite bricks based on zeolite-poor rock and Hen's eggshell, J. Build. Eng. 45 (2022), 103491, https://doi.org/10.1016/J.JOBE.2021.103491.
[45] J.E.F.M. Ibrahim, M. Tihtih, L.A. Gömze, Environmentally-friendly ceramic bricks made from zeolite-poor rock and sawdust, Construct. Build. Mater. 297 (2021), 123715, https://doi.org/10.1016/j.conbuildmat.2021.123715.
[46] H. Huang, W. Qiu, O.K. Tan, W. Zhu, L.M. Zhou, Effect of excess TiO2 on the phase evolution and densification of sol-gel derived (Ba,Sr)TiO3 powders, J. Electroceram. 16 (2006) 337–341, https://doi.org/10.1007/s10832-006-9875-3.
[47] X. Wang, P. Ren, Q. Wang, H. Fan, G. Zhao, Dielectric, piezoelectric and conduction properties of yttrium acceptor-doped BaTiO3 ceramics, J. Mater. Sci. Mater. Electron. 27 (2016) 11762–11769, https://doi.org/10.1007/S10854-016-5315-6/FIGURES/6.
[48] Q. Sun, J. Hu, Q. Gu, K. Bian, J. Wang, K. Xiong, K. Zhu, Sol-hydrothermal synthesis, crystal structures and excellent dielectric stability of yttrium doped BaTiO3 ceramics, 31, 2016, pp. 854–859, https://doi.org/10.1080/10667857.2016.1253265.
[49] I. Sakaguchi, S. Hirose, T. Furuta, K. Watanabe, K. Kageyama, S. Hishita, H. Haneda, N. Ohashi, Oxygen diffusion in rare-earth doped BaTiO3 ceramics, Key Eng. Mater. 582 (2014) 189–193, https://doi.org/10.4028/WWW.SCIENTIFIC.NET/KEM.582.189.
[50] G. Panomsuwan, H. Manuspiya, Structural and dielectric properties of sol–gel derived Ba1–xSrxTiO3 ($0 \leq x \leq 0.5$) ceramics for energy storage applications, Mater. Res. Express 6 (2018), 026310, https://doi.org/10.1088/2053-1591/AAEDF2.
[51] C.L. Freeman, J.A. Dawson, H.R. Chen, J.H. Harding, L. Bin Ben, D.C. Sinclair, A new potential model for barium titanate and its implications for rare-earth doping, J. Mater. Chem. 21 (2011) 4861–4868, https://doi.org/10.1039/C0JM04058D.
[52] R.A. Eichel, Defect structure of oxide ferroelectrics-valence state, site of incorporation, mechanisms of charge compensation and internal bias fields : IInvited review for, J. Electroceram., J. Electroceramics. 19 (2007) 9–21, https://doi.org/10.1007/S10832-007-9068-8/FIGURES/7.
[53] S. Lee, W.H. Woodford, C.A. Randall, Crystal and defect chemistry influences on band gap trends in alkaline earth perovskites, Appl. Phys. Lett. 92 (2008), 201909, https://doi.org/10.1063/1.2936091.
[54] M. Ferrari, L. Lutterotti, Method for the simultaneous determination of anisotropic residual stresses and texture by x-ray diffraction, J. Appl. Phys. 76 (1998) 7246, https://doi.org/10.1063/1.358006.
[55] M.A. Basyooni, M. Al-Dossari, S.E. Zaki, Y.R. Eker, M. Yilmaz, M. Shaban, Tuning the metal–insulator transition properties of VO2 thin films with the synergetic combination of oxygen vacancies, strain engineering, and tungsten doping, nanomater, 12, 2022, p. 1470, https://doi.org/10.3390/NANO12091470.
[56] M. Shaban, G.F. Attia, M.A. Basyooni, H. Hamdy, Morphological and structural properties of spin coated tin oxide thin films, Int. J. Eng. Adv. Res. Technol. 1 (2015) 11–14.
[57] A. King, R. Singh, R. Anand, S.K. Behera, B.B. Nayak, Phase and luminescence behaviour of Ce-doped zirconia nanopowders for latent fingerprint visualisation, Optik 242 (2021), https://doi.org/10.1016/j.ijleo.2021.167087.
[58] S.E. Zaki, M.A. Basyooni, M. Shaban, M. Rabia, Y.R. Eker, G.F. Attia, M. Yilmaz, A. M. Ahmed, Role of oxygen vacancies in vanadium oxide and oxygen functional groups in graphene oxide for room temperature CO 2 gas sensors, Sensors Actuators, A Phys. 294 (2019) 17–24, https://doi.org/10.1016/j.sna.2019.04.037.
[59] G. Choi, A.H. Choi, L.A. Evans, S. Akyol, B. Ben-Nissan, A review: recent advances in sol-gel-derived hydroxyapatite nanocoatings for clinical applications, J. Am. Ceram. Soc. 103 (2020) 5442–5453, https://doi.org/10.1111/jace.17118.
[60] M. Ganguly, S.K. Rout, C.W. Ahn, I.W. Kim, M. Kar, Structural, electrical and optical properties of Ba(Ti1−xYb4x/3)O3 ceramics, Ceram. Int. 39 (2013) 9511–9524, https://doi.org/10.1016/J.CERAMINT.2013.05.070.
[61] K. Niesz, T. Ould-Ely, H. Tsukamoto, D.E. Morse, Engineering grain size and electrical properties of donor-doped barium titanate ceramics, Ceram. Int. 37 (2011) 303–311, https://doi.org/10.1016/j.ceramint.2010.08.040.
[62] T. Badapanda, S. Sarangi, B. Behera, S. Parida, S. Saha, T.P. Sinha, R. Ranjan, P. K. Sahoo, Optical and dielectric study of strontium modified barium zirconium titanate ceramic prepared by high energy ball milling, J. Alloys Compd. 645 (2015) 586–596, https://doi.org/10.1016/J.JALLCOM.2015.05.005.
[63] H.Y. Tian, W.G. Luo, X.H. Pu, X.Y. He, P.S. Qiu, A.L. Ding, S.H. Yang, D. Mo, Determination of the optical properties of sol-gel-derived BaxSr1-xTiO3 thin film by spectroscopic ellipsometry, J. Phys. Condens. Matter 13 (2001) 4065, https://doi.org/10.1088/0953-8984/13/18/314.

[64] S. Parida, A. Satapathy, E. Sinha, A. Bisen, S.K. Rout, Effect of neodymium on optical bandgap and microwave dielectric properties of barium zirconate ceramic, Metall. Mater. Trans. A Phys. Metall. Mater. Sci. 46 (2015) 1277–1286, https://doi.org/10.1007/S11661-014-2725-Z/TABLES/3.

[65] R.E.A. Ngida, M.F. Zawrah, R.M. Khattab, E. Heikal, Hydrothermal synthesis, sintering and characterization of nano La-manganite perovskite doped with Ca or Sr, Ceram. Int. 45 (2019) 4894–4901, https://doi.org/10.1016/J.CERAMINT.2018.11.188.

[66] Y. He, Heat capacity, thermal conductivity, and thermal expansion of barium titanate-based ceramics, Thermochim. Acta 419 (2004) 135–141, https://doi.org/10.1016/j.tca.2004.02.008.

[67] T.T. Khan, S.C. Ur, Thermoelectric properties of the yttrium-doped ceramic oxide SrTiO3, J. Kor. Phys. Soc. 701 (70) (2017) 93–97, https://doi.org/10.3938/JKPS.70.93.

[68] H. Muta, K. Kurosaki, S. Yamanaka, Thermoelectric properties of doped BaTiO3-SrTiO3 solid solution, J. Alloys Compd. 368 (2004) 22–24, https://doi.org/10.1016/j.jallcom.2003.07.016.

[69] H. Muta, K. Kurosaki, S. Yamanaka, Thermoelectric properties of rare earth doped SrTiO3, J. Alloys Compd. 350 (2003) 292–295, https://doi.org/10.1016/S0925-8388(02)00972-6.

[70] J. Liu, C.L. Wang, Y. Li, W.B. Su, Y.H. Zhu, J.C. Li, L.M. Mei, Influence of rare earth doping on thermoelectric properties of SrTiO3 ceramics, J. Appl. Phys. 114 (2013), 223714, https://doi.org/10.1063/1.4847455.

[71] A.I. Hussein, A.N.C. Mat, N.A.A. Abd Wahab, I. Ab Rahman, A. Husein, Z. Ab-Ghani, Synthesis and properties of novel calcia-stabilized zirconia (Ca-SZ) with nano calcium oxide derived from cockle shells and commercial source for dental application, Appl. Sci. 10 (2020), https://doi.org/10.3390/APP10175751.